

## Supporting Information

### An Electronically-Driven Improper Ferroelectric: Tungsten Bronzes as Microstructural Analogues for the Hexagonal Manganites

Jason A. McNulty<sup>1</sup>, T. Thao Tran<sup>2</sup>, P. Shiv Halasyamani<sup>2</sup>, Shane J. McCartan<sup>3</sup>, Ian MacLaren<sup>3</sup>, Alexandra S. Gibbs<sup>4</sup>, Felicia J. Y. Lim<sup>5,6</sup>, Patrick W. Turner<sup>5</sup>, J. Marty Gregg<sup>5</sup>, Philip Lightfoot<sup>1</sup>, Finlay D. Morrison<sup>1,\*</sup>.

<sup>1</sup>School of Chemistry, University of St Andrews, St Andrews KY16 9ST, UK.

<sup>2</sup>Department of Chemistry, University of Houston, 3585 Cullen Blvd, 112 Fleming Building, Houston, TX 77204-5003, USA.

<sup>3</sup>School of Physics and Astronomy, University of Glasgow, Glasgow G12 8QQ, UK.

<sup>4</sup>ISIS Facility, Rutherford Appleton Laboratory, Chilton, Didcot, OX11 0QX, UK.

<sup>5</sup>Department of Mathematics and Physics, Queens University, University Rd., Belfast BT7 1NN, UK.

<sup>6</sup>Department of Mechanical Engineering, University of Sheffield, Sheffield S3 7QB, UK.

#### S1. Structural analysis

All Rietveld refinements were carried out using the General Structure Analysis System (GSAS) software package<sup>1,2</sup>. A 12-term shifted Chebyshev background function was used to account for background coefficients. Parameters refined were lattice parameters, atomic positions, isotropic atomic displacement parameters, zero point, profile coefficients and phase fractions, where applicable. Displacement parameters were constrained to be the same for each atom type. Small peaks from the vanadium can were identified in all PND patterns; these were not included in the refinements. In all diagrams containing refinement profiles, observed data are indicated by crosses, fitted intensity by solid red lines, background in green and difference profile in blue. Vertical tick marks indicate expected reflections.

Refinement of PND data (see main text and below) indicates that CsNbW<sub>2</sub>O<sub>9</sub> adopts the high symmetry *P6/mmm* aristotype at high temperature and undergoes sequential phase transitions involving: a) cell tripling in *ab* at  $T < 1100$  K; b) *c*-axis doubling below *ca.* 355 K; and c) an orthorhombic distortion below *ca.* 300 K. The group-subgroup relations indicate several possible phase transition sequences.

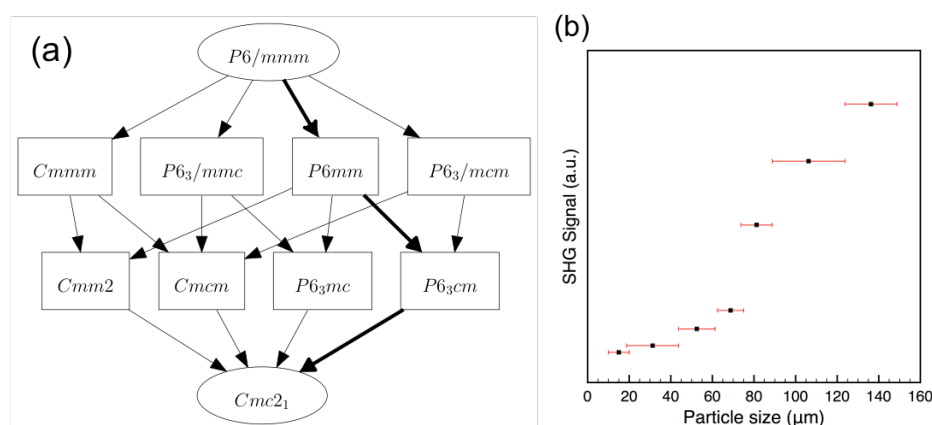


**Figure S1.** (a) Group-subgroup relations<sup>3</sup> for CsNbW<sub>2</sub>O<sub>9</sub> hexagonal tungsten bronze obtained from the Bilbao Crystallographic Server<sup>4-6</sup>; (b) phase matchable SHG signal ( $280 \times \alpha$ -SiO<sub>2</sub>) at room temperature indicating CsNbW<sub>2</sub>O<sub>9</sub> is polar at room temperature, ruling out *Cmmm*, *Cmcm*, *P6<sub>3</sub>/mmc* and *P6<sub>3</sub>/mcm* space groups. The symmetry breaking sequence as determined by Rietveld refinement of PND data (see main text and below) is indicated by the bold lines.

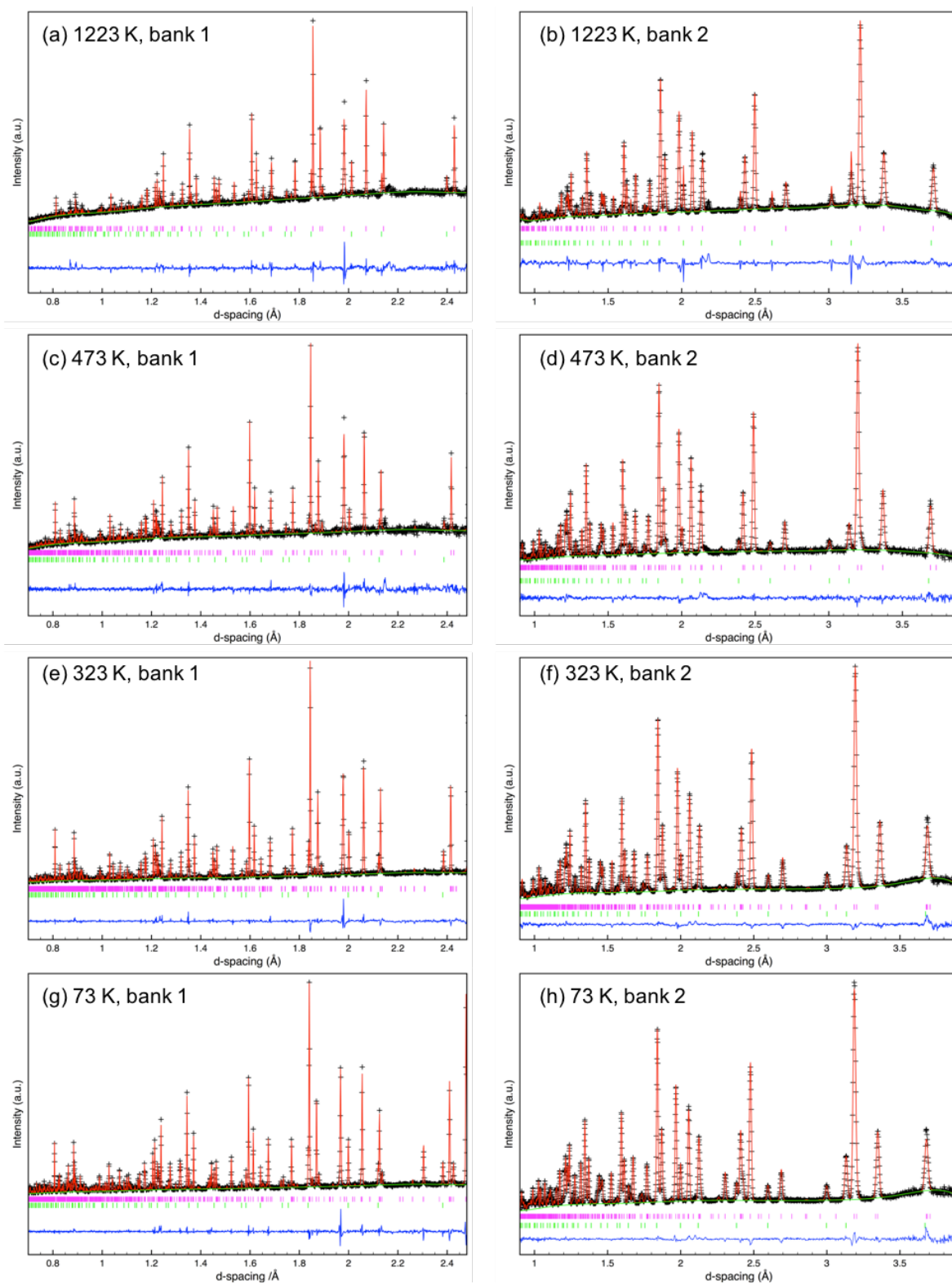


**Figure S2:** Full Rietveld refinement profiles of PND data at selected temperatures in space groups: (a, b) high symmetry  $P6/mmm$  aristotype ( $h$ - $\text{WO}_3$  structure); (c, d)  $P6mm$  with cell with tripling in  $ab$ ; (e, f)  $c$ -axis doubled  $P6_3cm$  (see Table S2 for justification for selection over  $P6_3mc$ ); and (g, h) orthorhombic  $Cmc2_1$ . Unit cell dimensions and goodness-of-fit parameters at all temperatures are collated in Table S1.

**Table S1.** Temperature dependence of absolute<sup>†</sup> and reduced<sup>‡</sup> unit cell dimensions, goodness-of-fit parameters and phase fraction (P) of HTB phase compared to that of the CsNbWO<sub>6</sub> defect pyrochlore secondary phase, as determined from Rietveld refinement of PND data.

T /K	<i>a</i> /Å	<i>a</i> <sub>HTB</sub> /Å	<i>b</i> /Å	<i>b</i> <sub>HTB</sub> /Å	<i>c</i> /Å	<i>c</i> <sub>HTB</sub> /Å	Cell Vol /Å <sup>3</sup>	χ <sup>2</sup>	wRp /%	Rp /%	P /wt%
73	22.0867 (3)	7.3622	12.7431 (2)	7.3572	7.8664 (1)	3.9332	2214.03 (4)	3.478	3.18	3.26	86.87
123	22.0900 (3)	7.3633	12.7481 (2)	7.3601	7.8731 (1)	3.9366	2217.14 (4)	3.909	3.35	3.36	86.77
173	22.0953 (4)	7.3651	12.7540 (3)	7.3635	7.8812 (1)	3.9406	2220.97 (4)	3.651	3.25	3.26	86.65
223	22.1024 (5)	7.3675	12.7607 (3)	7.3674	7.8901 (1)	3.9451	2225.35 (4)	3.511	3.18	3.21	86.86
273	22.1131 (6)	7.3710	12.7665 (4)	7.3707	7.8993 (1)	3.9497	2230.02 (4)	3.403	3.13	3.10	86.92
298	22.1184 (6)	7.3728	12.7696 (3)	7.3725	7.9037 (1)	3.9519	2232.36 (4)	6.059	2.95	2.76	87.09
323	12.7731 (1)	7.3746	12.7731 (1)	7.3746	7.9082 (1)	3.9541	1117.37 (2)	6.958	3.18	2.90	87.28
338	12.7749 (1)	7.3756	12.7749 (1)	7.3756	7.9104 (1)	3.9552	1118.01 (2)	6.572	3.09	2.86	87.11
348	12.7758 (1)	7.3761	12.7758 (1)	7.3761	7.9113 (1)	3.9557	1118.29 (2)	6.518	3.07	2.77	87.02
363	12.7769 (1)	7.3767	12.7769 (1)	7.3767	3.9561 (1)	3.9561	559.30 (1)	6.835	3.15	2.81	87.16
373	12.7776 (1)	7.3772	12.7776 (1)	7.3772	3.9562 (1)	3.9562	559.39 (1)	6.731	3.12	2.76	87.2
473	12.7848 (2)	7.3813	12.7848 (2)	7.3813	3.9608 (1)	3.9608	560.66 (2)	1.961	2.88	2.85	90.34
673	12.7975 (2)	7.3886	12.7975 (2)	7.3886	3.9632 (1)	3.9632	562.12 (2)	1.979	2.89	2.87	89.74
873	12.8122 (2)	7.3971	12.8122 (2)	7.3971	3.9657 (1)	3.9657	563.76 (2)	1.957	2.86	2.75	90.38
923	12.8159 (2)	7.3993	12.8159 (2)	7.3993	3.9661 (1)	3.9661	564.15 (2)	5.182	2.34	1.96	90.14
973	12.8201 (2)	7.4017	12.8201 (2)	7.4017	3.9666 (1)	3.9666	564.59 (2)	5.104	2.31	1.91	90.47
1023	12.8245 (2)	7.4042	12.8245 (2)	7.4042	3.9670 (1)	3.9670	565.03 (2)	5.185	2.32	1.89	90.53
1073	12.8292 (2)	7.4069	12.8292 (2)	7.4069	3.9670 (1)	3.9670	565.45 (2)	5.140	2.31	1.92	90.97
1123	7.4107 (1)	7.4107	7.4107 (1)	7.4107	3.9665 (1)	3.9665	188.65 (1)	8.902	3.04	2.16	88.97
1173	7.4145 (1)	7.4145	7.4145 (1)	7.4145	3.9651 (1)	3.9651	188.78 (1)	8.328	2.94	2.14	88.82
1223	7.4195 (1)	7.4195	7.4195 (1)	7.4195	3.9624 (1)	3.9624	188.90 (1)	8.933	3.05	2.12	86.44

<sup>†</sup>Numbers in parentheses indicate standard deviations of the refined parameters, in units of the least-significant figures, as estimated in the GSAS software<sup>1,2</sup>.

<sup>‡</sup>cell dimensions reduced relative to the *P6/mmm* aristotype with dimensions *a*<sub>HTB</sub> ≈ 7.4 Å and *c*<sub>HTB</sub> ≈ 3.9 Å: *P6mm* *a* = √3*a*<sub>HTB</sub>, *c* = *c*<sub>HTB</sub>; *P6<sub>3</sub>cm* *a* = √3 *a*<sub>HTB</sub>, *c* = 2 *c*<sub>HTB</sub>; *Cmc2<sub>1</sub>* *a* = 3 *a*<sub>HTB</sub>, *b* = √3 *a*<sub>HTB</sub>, *c* = 2 *c*<sub>HTB</sub>.

**Table S2:** Goodness-of-fit parameters obtained from PND data at 348K and refined in both *P6<sub>3</sub>cm* and *P6<sub>3</sub>mc* hexagonal space groups corresponding to *c*-axis doubling. The data fit better to the *P6<sub>3</sub>cm* structure despite fewer refineable parameters (*N*<sub>ref</sub>) compared to *P6<sub>3</sub>mc*. It is also worthy to note that *P6<sub>3</sub>mc* requires introduction of an *A*<sub>4</sub><sup>+</sup> mode which is unfavourable as it requires breaking of the corner linkages as discussed by Whittle *et al.*<sup>7</sup>

T (K)	<i>P6<sub>3</sub>cm</i>				<i>P6<sub>3</sub>mc</i>			
	χ <sup>2</sup>	wRp (%)	Rp (%)	<i>N</i> <sub>ref</sub>	χ <sup>2</sup>	wRp (%)	Rp (%)	<i>N</i> <sub>ref</sub>
348	6.538	3.08	2.76	81	6.938	3.17	2.82	83
338	6.593	3.10	2.85	81	7.047	3.20	2.92	83
323	6.951	3.17	2.91	81	7.467	3.29	2.98	83

## S2. Pyrochlore secondary phase

A small amount of the defect pyrochlore CsNbWO<sub>6</sub> (ICSD Collection Code 15699) was observed in the ‘stoichiometric’ CsNbW<sub>2</sub>O<sub>9</sub> sample. The amount, as determined from Rietveld refinement, remains constant at 10-12 wt% at all temperatures. 10% deficiency of Cs at the A-site (and with compensated Nb:W ratio to maintain charge balance, Cs<sub>0.9</sub>Nb<sub>0.9</sub>W<sub>2.1</sub>O<sub>9</sub>) removes the unwanted secondary defect pyrochlore CsNbWO<sub>6</sub> phase, Fig S2. Single (HTB) Cs<sub>0.9</sub>Nb<sub>0.9</sub>W<sub>2.1</sub>O<sub>9</sub> phase adopts the same structure as the main HTB phase in CsNbW<sub>2</sub>O<sub>9</sub> sample as determined by PND at ambient temperature. Although variable temperature PND was not available for Cs<sub>0.9</sub>Nb<sub>0.9</sub>W<sub>2.1</sub>O<sub>9</sub>, PXRD data (not shown) indicate that the lattice parameters show the same temperature dependence as Fig 2a in the main text, with a similar drop in the *c*-axis observed at *ca.* 1100 K. Cs<sub>0.9</sub>Nb<sub>0.9</sub>W<sub>2.1</sub>O<sub>9</sub> also displays a comparable SHG signal, Fig S3.

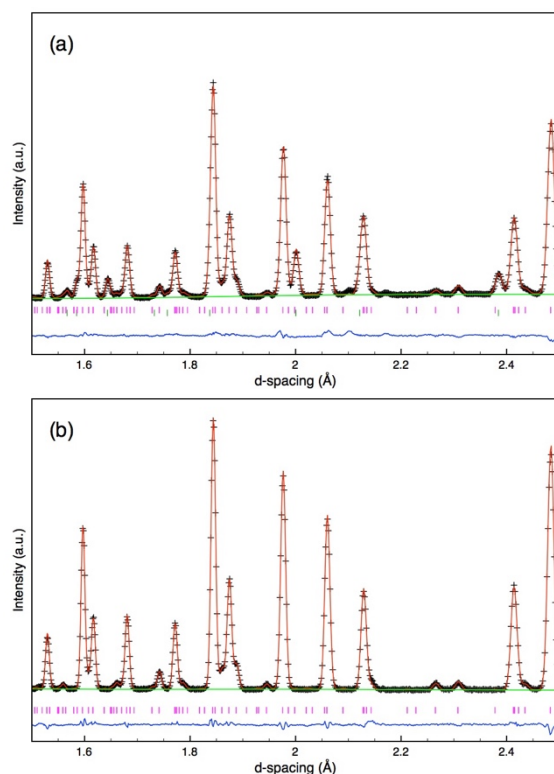


**Figure S3.** Refinement profiles of PND data obtained at room temperature for (a)  $\text{CsNbW}_2\text{O}_9$  ( $\chi^2 = 6.059$ ,  $wRp = 2.95\%$ ,  $Rp = 2.76\%$ ) and (b)  $\text{Cs}_{0.9}\text{Nb}_{0.9}\text{W}_{2.1}\text{O}_9$  ( $\chi^2 = 2.942$ ,  $wRp = 3.60\%$ ,  $Rp = 3.90\%$ ). The defect pyrochlore secondary phase (lower tickmarks) is not evident in (b) – note the absence of any intensity at *ca.* 2.39 Å. The main HTB phase is refined in  $Cmc2_1$  in both cases.

### S3 Second Harmonic Generation (SHG) Measurements

Powder SHG measurements were performed on a modified Kurtz-nonlinear optical (NLO) system using a pulsed Nd:YAG Quantel Ultra laser with a wavelength of 1064 nm. A detailed description of the methodology has been published.<sup>8</sup> As the powder SHG efficiency has been shown to strongly depend on particle size,<sup>9</sup> The material was ground and sieved into distinct particle size ranges (<20, 20–45, 45–63, 63–75, 75–90, >90 μm). Relevant comparisons with known SHG materials were made by grinding and sieving crystalline  $\alpha\text{-SiO}_2$  into the same particle size ranges. No index matching fluid was used in any of the experiments.

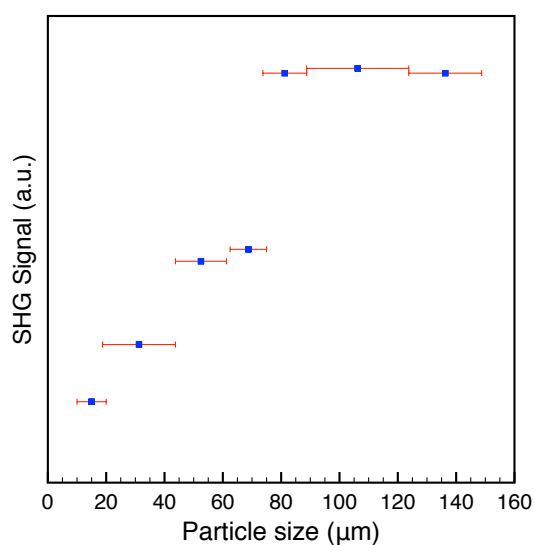


**Figure S4.** SHG data for ‘non-stoichiometric’  $\text{Cs}_{0.9}\text{Nb}_{0.9}\text{W}_{2.1}\text{O}_9$  indicating that this material is also non-centrosymmetric. The SHG signal ( $280 \times \alpha\text{-SiO}_2$ ) is comparable with that observed for ‘stoichiometric’  $\text{CsNbW}_2\text{O}_9$ .

#### S4. Destabilisation of SOJT

As discussed in the main text, the mechanism of symmetry breaking is purely displacive indicating that  $\text{CsNbW}_2\text{O}_9$  is an electronically-driven improper ferroelectric. The  $K_3$  mode is driven by the second order Jahn-Teller (SOJT) effect due to orbital mixing of the  $\text{Nb}^{5+}4d$  and  $\text{O}^{2-}2p$  orbitals. This is supported by the observation that on reduction of the amount of Nb present at the B-site either by Ta-doping ( $\text{Cs}_{0.9}\text{Nb}_{0.9-x}\text{Ta}_x\text{W}_{2.1}\text{O}_9$ ) or ‘W-doping’ (with concomitant A-site deficiency for charge balance:  $\text{Cs}_{0.9-x}\text{Nb}_{0.9-x}\text{W}_{2.1+x}\text{O}_9$ ) the displacive cell tripling  $K_3$  mode is destabilised. Fig S5 shows the broadening and disappearance of the (401) cell-tripling reflection with increasing  $x$  for both solid solutions outlined above.

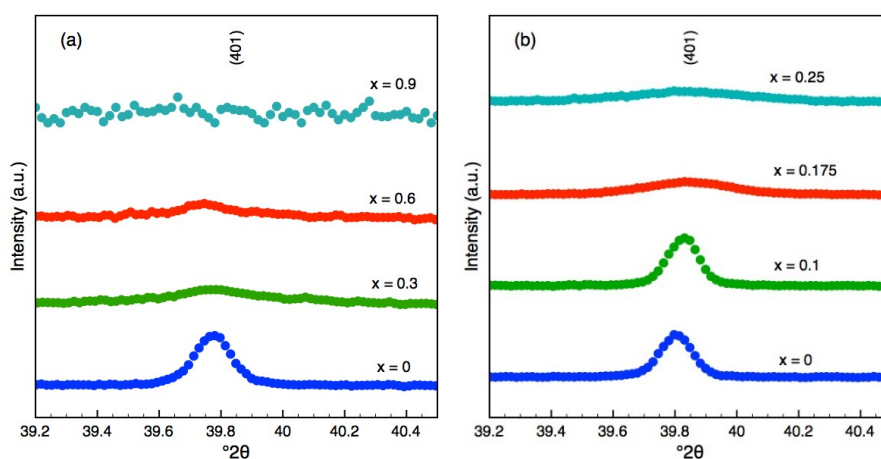


**Fig S5.** Room temperature PXRD data showing the intensity of the (401) cell-tripling reflection as a function of  $x$  in: (a)  $\text{Cs}_{0.9}\text{Nb}_{0.9-x}\text{Ta}_x\text{W}_{2.1}\text{O}_9$  and (b)  $\text{Cs}_{0.9-x}\text{Nb}_{0.9-x}\text{W}_{2.1+x}\text{O}_9$ . The concentration of Nb at the B-site is inversely proportional to  $x$ . All data have been normalised to the most intense (non-cell tripling) reflection.

## S5. Electrical and ceramic microstructure.

The electrical microstructure of  $\text{CsNbW}_2\text{O}_9$  was analysed by immittance spectroscopy over the temperature range ambient to *ca.* 600 K. Data were collected from 5 Hz to 13 MHz using an HP 4129A impedance analyser with an *ac* excitation of 100 mV. Data were analysed using the ZView software suite. Below *ca.* 400 K samples were too resistive ( $> 10^7 \text{ M}\Omega\text{cm}$ ) to observe any relaxation. At higher temperatures a single semi-circular arc was observed in the complex impedance ( $Z^*$ ) plane plot (Fig S6a); this arc had an associated capacitance of *ca.* 10-15 pF over the temperature range studied and corresponds to the bulk response<sup>10</sup>. The complex modulus ( $M^*$ ) plane plot indicated two convoluted semi-circular arcs as evident from the high degree of asymmetry at high frequency, Fig S6b. The smaller, high frequency arc is more clearly evident as a shoulder in the imaginary modulus  $M''$  spectroscopic plot, Fig S6c; this shoulder is attributed to the defect pyrochlore secondary phase as it is not evident in the ‘non-stoichiometric’  $\text{Cs}_{0.9}\text{Nb}_{0.9}\text{W}_{2.1}\text{O}_9$  sample (not shown). The main arc in both the  $Z^*$  and  $M^*$  plots have the same relaxation time (evident from the coincidental peak maxima in the combined imaginary impedance ( $Z''$ ) and modulus ( $M''$ ) spectroscopic plot (Fig S6d). There is no evidence of any significant grain boundary response and the data are dominated by the bulk HTB response. The fixed frequency capacitance and loss data in Fig 2b therefore represents the bulk response.

The bulk conductivity extracted from  $Z^*$  plots exhibit Arrhenius behaviour, Fig S7, with an activation energy of *ca.* 0.76 eV, which given the off-white colour of samples, is clearly not intrinsic but is likely associated with defect states such as oxygen vacancies which are ubiquitous in inorganic oxides. No low frequency spike associated with ionic conductivity was observed in any of the complex impedance data.

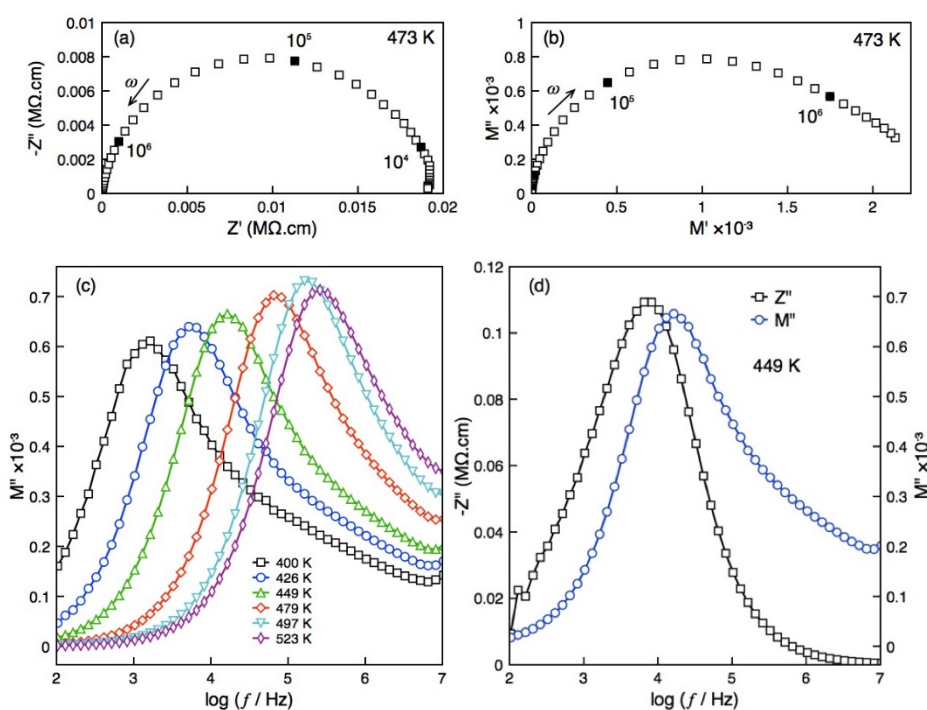


**Fig S6.** Complex impedance,  $Z^*$ , (a) and complex modulus,  $M^*$ , (b) plane plots of data collected at 473 K for  $\text{CsNbW}_2\text{O}_9$ ; selected frequencies (in Hz) are indicated by filled symbols. Spectroscopic plot of imaginary modulus ( $M''$ ) as a function of temperature (c); combined imaginary modulus ( $M''$ ) and impedance ( $Z''$ ) spectroscopic plot at 449 K. All data are uncorrected for sample geometry; the sample geometric factor ( $d/A$  where  $d$  is the sample thickness and  $A$  is the electrode area) is  $0.286 \text{ cm}^{-1}$ .

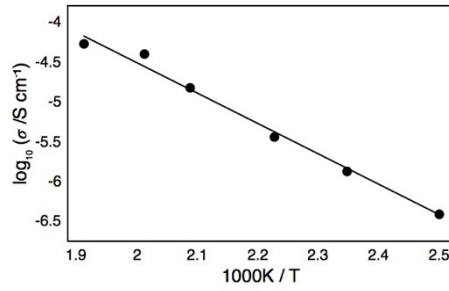


**Fig S7.** Arrhenius plot of bulk conductivity of CsNbW<sub>2</sub>O<sub>9</sub> extracted from complex impedance plane plots.

Scanning electron microscopy (SEM - Jeol JSM 5600) of fractured pellet surfaces indicated a bimodal grain size with larger (~ 20 μm) grains in a finer-grained (~ 1-2 μm) matrix, Fig S8. Significant porosity is evident and, based on volume and mass measurements, pellet densities were estimated to be *ca.* 83% of theoretical density.

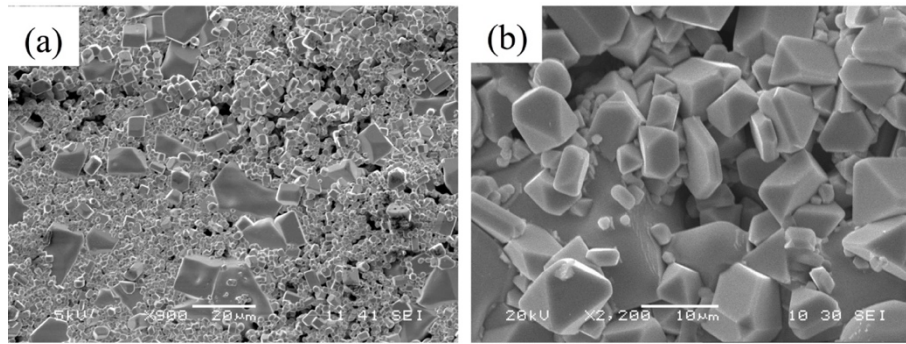


**Figure S8.** SEM micrographs of CsNbW<sub>2</sub>O<sub>9</sub> pellet fracture surfaces indicating a fine grained matrix with larger grains embedded and the presence of significant porosity.

### S6. Polarisation calculations and P-E measurements

The theoretical total polarisation in the polar *c*-axis,  $P_z$ , based on the structural refinements was calculated through summation of the individual ion contributions following the methodology of Shimakawa *et al.*:<sup>11</sup>

$$P_z = \frac{\sum_i (m_i \cdot \Delta z_i \cdot Q_i e)}{V}$$

where  $m_i$  is the site multiplicity,  $\Delta z_i$  is the displacement along the *c*-axis compared to the non-polar co-ordinate, and  $Q_i e$  is the ionic charge (in Coulombs) of each *i* ion and  $V$  is the unit cell volume. The results obtained at room temperature are shown in Fig S9 and indicate that the total net polarisation is of the order 12 μC/cm<sup>2</sup> and that the largest contribution comes from the B1-site.

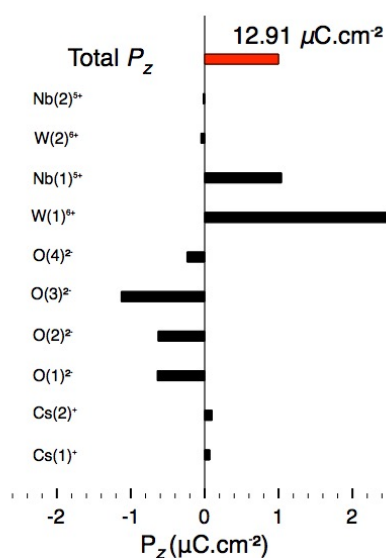


**Fig S9.** Schematic of the individual ion contributions to the total polarisation in the polar  $c$ -axis,  $P_z$ . Note that for clarity only the individual ion contributions are to scale; the magnitude of the total polarisation (red bar) is given numerically in the figure.

Attempts to collect polarisation-field hysteresis measurements were carried out between 50 and 475 K using an aixACCT TF2000 analyser fitted with a TREK 4kV amplifier. No evidence of ferroelectric switching was observed under the conditions used. The data indicate a lossy linear dielectric response at fields up to *ca.* 30 kV/cm (Fig S10). The lack of saturation and polarisation switching is likely a result of poor ceramic microstructure.

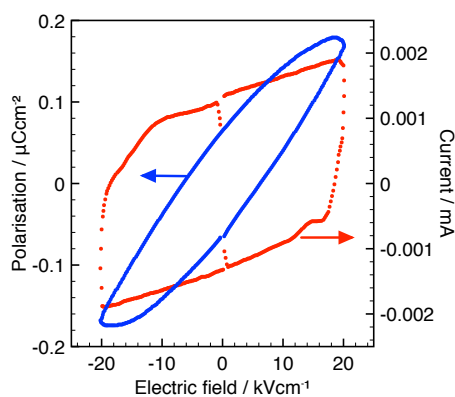


**Fig S10.** Polarisation-electric field (P-E) response for CsNbW<sub>2</sub>O<sub>9</sub> recorded at 425 K under an applied field of 20 kV/cm and at 1.75 kHz.

## S7. Transmission Electron Microscopy

It is worth noting that although the material undergoes a transition to orthorhombic at  $\sim 300\text{K}$ , it was decided to index the diffraction pattern using the hexagonal system. Therefore, although our indexing in the given diffraction pattern (Fig 4b of the main manuscript) is self-consistent, other indexings are also possible. Due to the extremely small distortions of the unit cell and the fact that unique directions in the orthorhombic cell are only revealed by the appearance of extra superlattice spots in a very small number of zone axis diffraction patterns, determination of unique directions in the orthorhombic system was not possible using conventional selected area diffraction methods. Consequently, the hexagonal cell was used. Obviously indexing the diffraction pattern (Fig 4b) as  $[0\bar{2}2\bar{9}]$  is one of several crystallographically equivalent variants within the hexagonal structure and these cover even more variants within the orthorhombic structure.

## References

- 1 Larson, A. C. & Von Dreele, R. B. General Structure Analysis System (GSAS). 86-748 (2000).
- 2 Toby, B. H. EXPGUI, a graphical user interface for GSAS. *Journal of Applied Crystallography* **34**, 210-213, doi:10.1107/s0021889801002242 (2001).
- 3 Ivantchev, S., Kroumova, E., Madariaga, G., Pérez-Mato, J. M. & Aroyo, M. I. SUBGROUPGRAPH: a computer program for analysis of group–subgroup relations between space groups. *Journal of Applied Crystallography* **33**, 1190-1191, doi:10.1107/s0021889800007135 (2000).
- 4 Aroyo, M. I. *et al.* Crystallography online: Bilbao Crystallographic Server. *Bulgarian Chemical Communications* **43**, 183-197 (2011).
- 5 Aroyo, M. I. *et al.* Bilbao Crystallographic Server: I. Databases and crystallographic computing programs. *Zeitschrift für Kristallographie - Crystalline Materials* **221**, doi:10.1524/zkri.2006.221.1.15 (2006).
- 6 Aroyo, M. I., Kirov, A., Capillas, C., Perez-Mato, J. M. & Wondratschek, H. Bilbao Crystallographic Server. II. Representations of crystallographic point groups and space groups. *Acta Crystallogr A* **62**, 115-128, doi:10.1107/S0108767305040286 (2006).
- 7 Whittle, T. A., Schmid, S. & Howard, C. J. Octahedral tilting in the tungsten bronzes. *Acta Crystallogr B Struct Sci Cryst Eng Mater* **71**, 342-348, doi:10.1107/S2052520615008252 (2015).
- 8 Ok, K. M., Chi, E. O. & Halasyamani, P. S. Bulk characterization methods for non-centrosymmetric materials: second-harmonic generation, piezoelectricity, pyroelectricity, and ferroelectricity. *Chem Soc Rev* **35**, 710-717, doi:10.1039/b511119f (2006).
- 9 Kurtz, S. K. & Perry, T. T. A Powder Technique for the Evaluation of Nonlinear Optical Materials. *Journal of Applied Physics* **39**, 3798-3813, doi:10.1063/1.1656857 (1968).
- 10 Irvine, J. T. S., Sinclair, D. C. & West, A. R. Electroceramics: Characterization by Impedance Spectroscopy. *Advanced Materials* **2**, 132-138, doi:10.1002/adma.19900020304 (1990).
- 11 Shimakawa, Y. *et al.* Crystal structure and ferroelectric properties of  $ABi_2Ta_2O_9$  (A = Ca, Sr, and Ba). *Physical Review B* **61**, 6559-6564, doi:10.1103/PhysRevB.61.6559 (2000).